Research in Astronomy and Astrophysics, 25:015012 (18pp), 2025 January

https://doi.org/10.1088/1674-4527/ad9197
CSTR: 32081.14.RAA.ad9197

The LAMOST Spectroscopic Survey of Supergiants in M31 and M33

Hao Wu[1,2], Yang Huang[3,4,8], Huawei Zhang[1,2,8], Haibo Yuan[5,6], Zhiying Huo[4], and Cheng Liu[7]
[1] Department of Astronomy, School of Physics, Peking University, Beijing 100871, China; zhanghw@pku.edu.cn
[2] Kavli Institute for Astronomy and Astrophysics, Peking University, Beijing 100871, China
[3] School of Astronomy and Space Science, University of Chinese Academy of Science, Beijing 100049, China; huangyang@ucas.ac.cn
[4] National Astronomical Observatories, Chinese Academy of Sciences, Beijing 100101, China
[5] Institute for Frontiers in Astronomy and Astrophysics, Beijing Normal University, Beijing 102206, China
[6] Department of Astronomy, Beijing Normal University, Beijing 100871, China
[7] Department of Scientific Research, Beijing Planetarium, Beijing 100044, China
Received 2024 June 05; revised 2024 October 16; accepted 2024 November 05; published 2025 January 8

Abstract

We present systematic identifications of supergiants in M31/M33 based on the Large Sky Area Multi-Object Fiber Spectroscopic Telescope (LAMOST) spectroscopic survey. Radial velocities of nearly 5000 photometrically selected M31/M33 supergiant candidates have been properly derived from the qualified spectra released in LAMOST DR10. By comparing their radial velocities with those predicted from the rotation curve of M31, as well as utilizing Gaia astrometric measurements to exclude foreground contaminations, 199 supergiant members in M31, including 168 "Rank1" and 31 "Rank2," have been successfully identified. This sample contains 62 blue supergiants (BSGs, all "Rank1"), 134 yellow supergiants (YSGs, 103 "Rank1" and 31 "Rank2") and three red supergiants (RSGs, all "Rank1"). For M33, we identify 84 supergiant members (56 "Rank1" and 28 "Rank2"), which include 28 BSGs (all "Rank1"), 53 YSGs (25 "Rank1" and 28 "Rank2") and three RSGs (all "Rank1"). So far, this is one of the largest supergiant samples of M31/M33 with full optical wavelength coverage ($3700 < \lambda < 9100$ Å). This sample is valuable for understanding star formation and stellar evolution under different environments.

Key words: galaxies: individual (M31, M33) – galaxies: stellar content – (galaxies:) Local Group – stars: evolution – stars: massive – (stars:) supergiants

1. Introduction

Supergiants, as the evolutionary phases of massive stars ($>8\,M_{\odot}$), are extremely rare but of great interest because of their importance in constraining stellar evolutionary theory (e.g., Massey & Olsen 2003; Neugent et al. 2010; Massey et al. 2013; 2016) and their profound feedback effects to the overall evolution of their host galaxies (e.g., Oey & Clarke 2009). Several different evolutionary stages after the termination of the main sequence of massive stars can be classified according to their locations on the Hertzsprung–Russell (H-R) diagram (see Figure 1, where the evolutionary tracks are taken from Ekström et al. 2012). As shown in Figure 1, in the luminous blue range, blue supergiants (BSGs) are labeled, which are actually a mix of hot main sequence and other more evolved BSGs, including the evolved descendants of the most massive O-type stars: Wolf–Rayet stars (WRs). In addition, for the most luminous part of the blue region, the classical luminous blue variables (LBVs) phase will be the next stage of those most massive (e.g., $M > 30$–$60\,M_{\odot}$) main sequence stars, which exhibit spectacular eruptions with several magnitudes of enhancement visually and large mounts of material being ejected (see, e.g., Bohannan 1997; Conti 1997). In the central part of the H-R diagram, the region within the two black dashed lines as marked in Figure 1, yellow supergiants (YSGs) are labeled, which are F/G-type supergiants with effective temperature ($T_{\rm eff}$) roughly from 4800 to 7500 K and luminosity $\log L/L_{\odot} > 3.5$. The YSG is a short-lived stage, which can either evolve from main sequence massive stars or evolve back from red supergiants (RSGs) for stars with initial mass between 8 and 30 $M_{\odot}$. Finally, the RSG phases (K/M-type supergiants) are located in the cool (or red) region of the H-R diagram again as shown in Figure 1, which are relatively longer lived evolved descendants of moderately massive (8–25 $M_{\odot}$) stars. It is difficult to model the evolutionary tracks of massive stars, mainly due to the complicated mass loss process, which is still somewhat uncertain and lots of works (both theory and observation) are required to fully understand this process (e.g., Massey 2013; Smith 2014). The systematic search and study of supergiants in the Local Group (LG) of galaxies (perfect laboratories with simple variables: chemical compositions) will provide important clues to constraining the theoretical models of stellar evolution. In addition, the studies of supergiants in the LG galaxies will also help us to understand their profound

[8] Corresponding authors.

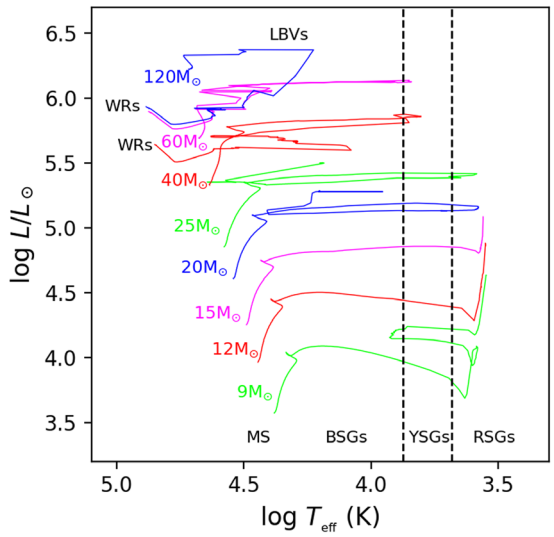

Figure 1. The evolutionary tracks of massive stars ($M > 8\,M_{\odot}$) for solar metallicity ($z = 0.014$) assuming an initial rotation velocity of 40% of the critical break-up speed taken from Geneva evolutionary tracks (Ekström et al. 2012). The evolutionary tracks with different initial masses are labeled with different colors. The two black vertical dashed lines represent the YSG region, located in $4800 < T_{\rm eff} < 7500$ K. Other evolutionary phases (BSGs, RSGs, WRs and LBVs) are also labeled at their corresponding locations.

feedback effects that affect the evolution of these LG galaxies themselves (reviewed by Oey & Clarke 2009).

To systematically identify the supergiants in LG galaxies, Massey et al. (2006, 2007) carried out the Local Group Galaxies Survey (LGGS) to obtain *UBVRI* photometry with precision better than 1%–2% for two spiral galaxies, M31 and M33, and for seven irregular galaxies IC 10, NGC 6822, WLM, Sextans A, Sextans B, Pegasus and Phoenix. With the precise photometry, one can select different types of supergiant candidates based on the color–magnitude or color–color diagrams. However, foreground contamination effectively hampers the selection of supergiants through only photometry, especially for YSGs. In addition, it is difficult to obtain accurate physical properties for those supergiants with photometry information available alone. Fortunately, spectroscopy can solve the above problems neatly. Using the Hectospec spectrograph equipped with 300 optical fibers mounted on the MMT 6.5 m telescope, systematic identifications of YSGs in M31 and of YSGs/RSGs in M33 were carried by Drout et al. (2009, 2012), respectively. Using the Hydra multi-object fiber spectrograph on the WIYN 3.5 m telescope, RSGs were systematically searched in M31 by Massey et al. (2009). Most recently, a more comprehensive search for supergiants in M31 and M33 was carried by Massey et al. (2016) by using the Hectospec spectrograph mounted on MMT. By combining former efforts, a large catalog of 700/1200 supergiant candidates of M31/M33 was constructed by Massey et al.(2016).

Although significant progresses have been made in searching for supergiants in M31/M33 in the past several years by Massey's group described above, the current supergiant sample of M31/M33 is still not complete because: (1) The number of photometrically selected supergiant candidates is quite large and hard to fully identify spectroscopically; (2) The wavelength coverage of current spectra does not include the full optical range and thus is not enough for further studies, such as metallicity estimates (Liu et al. 2022).

The Large Sky Area Multi-Object Fiber Spectroscopic Telescope (LAMOST, also named the Guoshoujing Telescope; Cui et al. 2012) is a 4 m quasi-meridian reflecting Schmidt telescope equipped with 4000 fibers, each with an angular diameter of 3.″3 projected on the sky, distributed in a circular field of view (FoV) of 5° in diameter. The LAMOST spectroscopic survey (Deng et al. 2012; Zhao et al. 2012; Liu et al. 2014) has a huge advantage in systematically searching for supergiants in M31/M33 given the fact that: (1) LAMOST is one of the telescopes with the highest rate of spectral acquisition. By the end of 2022, LAMOST had accumulated more than 21 million spectra, consisting of 11 million low resolution spectra (LRS) and 10 million medium resolution spectra (Yan et al. 2022); (2) The FoV of LAMOST is nearly the size of M31/M33; (3) The spectrographs used by the LAMOST spectroscopic survey yield spectra covering the whole optical range ($3700 < \lambda < 9100$ Å) with a moderately low resolution ($R \sim 1800$).

In this study, we present our systematic identification of supergiants in M31/M33 utilizing LAMOST Data Release 10 (DR10) data. Our approach involves the initial selection of photometric candidates through LGGS and Gaia photometry, which is described in Section 2. Subsequently, the spectroscopy from LAMOST and astrometry from Gaia are used to select true members in Section 3. In Section 4, we will show the results and provide some discussions. Finally, a summary is presented in Section 5.

2. Target Selection and Observations

As an extension of the LAMOST Spectroscopic Survey of the Galactic Anticentre (LSS-GAC. Liu et al. 2014), the M31 and M33 areas ($0° < \mathrm{R.A.} < 30°$ and $25° < \mathrm{decl.} < 50°$) were systematically observed by LAMOST. The detailed survey strategy and target selections are described in Yuan et al. (2015). In particular, potentially luminous M31/M33 sources (such as planetary nebulae, H II regions, globular clusters, and supergiant stars) and background quasars were observed with high priorities. In this work, we utilized LAMOST DR10 LRS data, which is a collection of spectra obtained from 2011 October to 2022 June. Here, our focus is on the supergiants in M31/M33 that are mainly located in the disk region of the two galaxies. Therefore, hereafter the M31/M33 area refers to about 3/1.5 square degrees around their centers (R.A. = 10.°68458, decl. = 41.°26875 for M31 and R.A. = 23.°46208, decl. = 30.°65994 for M33; Jarrett et al. 2003).

Here we introduce the detailed target selection of our supergiant candidates of M31/M33 in LAMOST DR10. First, the LGGS photometry catalog is cross-matched with LAMOST DR10, resulting in 1514 common sources for M31 and 981 ones for M33. Subsequently, by applying criteria from previous studies (mainly from Massey's group; e.g., Massey et al. 2006, 2009; Drout et al. 2009, 2012), the different types of supergiant candidates are selected as follows:

1. BSG (including WR and LBV) candidates:

$$Q = (U - B) - 0.72(B - V) \leqslant -0.6. \quad (1)$$

2. YSG candidates:

$$U - B > -0.4. \quad (2)$$

$$0.0 \leqslant B - V \leqslant 1.5. \quad (3)$$

3. RSG candidates:

$$V - R \geqslant 0.85. \quad (4)$$

$$B - V > -1.6(V - R)^2 + 4.18(V - R) - 0.83. \quad (5)$$

The greatest difficulty in selecting blue massive stars using photometry is the dust reddening. Though having negligible foreground extinction for the entire M31 [$E(B - V) = 0.06$] and M33 [$E(B - V) = 0.07$] (van den Bergh 2000), the inner dust of the two gas rich galaxies themselves will make those blue massive stars heavily and inhomogeneously reddened. The Johnson Q-index, as defined in Equation (1), is a reddening-free indicator (at least for $Q < -0.6$) of intrinsic color. This index can work effectively in selecting blue massive supergiants (Massey et al. 2016). For YSGs, the photometric cuts in Equations (2)–(3) only show their possible locations on a color–color diagram and a large number of foreground contaminations also unavoidably remain. The identifications of the real YSGs will highly rely on the results from spectroscopy or astrometry. The foreground contamination is also a challenge in identifying RSGs in M31/M33, but the color–color diagram (see Equation (5); Massey 1998; Drout et al. 2012), $B - V$ and $V - R$, can effectively distinguish RSGs and dwarfs, especially for $V - R > 0.6$. This is simply because $V - R$ is sensitive to effective temperature and $B - V$ is sensitive to both effective temperature and surface gravity.

The LGGS photometry has some caveats in selecting supergiant candidates: (1) The bright end of LGGS is not complete; (2) LGGS does not cover the entire M31/M33 sky region; (3) One or more bands of *UBVRI* are missing for some sources in the LGGS catalog. To address the first issue, we incorporated objects from Magnier et al. (1992) at the bright end. For the second and third cases, we utilized Gaia Data Release 3 (DR3) broadband $G/G_{\rm BP}/G_{\rm RP}$ photometry to select supergiant candidates using the criteria developed by Salomon et al. (2021). Notably, these criteria merely represent the positions of different types of supergiants on the color–color diagram, and candidates selected through this way may suffer a substantial number of foreground contaminants.

Table 1
Number of Supergiant Candidates of M31/M33 in LAMOST DR10 Selected Based on *UBVRI* Photometry

Galaxy	BSG Candidates	YSG Candidates	RSG Candidates
M31	108	908	6
M33	80	729	5

Note. Among the 924 YSG candidates in M31, 111 are selected based on photometry taken from Magnier et al. (1992) because those targets are too bright for LGGS.

Table 2
Number of LAMOST Supergiant Candidates in M31/M33 from LAMOST DR10 Selected Based on Gaia Photometry

Galaxy	BSG Candidates	YSG Candidates	RSG Candidates
M31	27	2230	1
M33	7	758	1

In addition to the above photometric criteria, three cuts related to LAMOST observations are applied. The first one requires V or G (for those without V photometry) magnitude to be brighter than 20 to match the limiting magnitude of LAMOST. The second one requires no nearby stars within $4''.00$ (similar to the diameter of the LAMOST fiber) of the supergiant candidates, or if there are any, they should be at least 2 mag fainter, so as to exclude contaminants from close bright neighbors. The last cut requires the spectral signal-to-noise ratio (SNR) to be greater than 5, ensuring the quality of the spectrum for subsequent analysis. Finally, we excluded the contaminants from M31/M33's extended sources, i.e., globular clusters, planetary nebulae, and H II regions, by cross-matching with catalogs from Chen et al. (2015), the M31 Revised Bologna Clusters and Candidates Catalog (Galleti et al. 2004, 2007, 2009) and Sarajedini & Mancone (2007), as well as catalogs from Yuan et al. (2010), Azimlu et al. (2011), Sanders et al. (2012), Zhang et al. (2020), Hodge et al. (1999) and Ciardullo et al. (2004).

The number of M31/M33 supergiant candidates is summarized in Tables 1 and 2. The number of RSG candidates is very small due to their intrinsically faint luminosities, which is out of the observation ability of LAMOST. The large number of YSG candidates is as expected since the photometric colors cannot distinguish YSGs with (a large number of) foreground contaminants.

3. Supergiant Identification

Here we introduce our methods for separating M31/M33 supergiants from foreground dwarfs. As mentioned earlier,

separating M31/M33 supergiants from foreground dwarfs based solely on their positions on the color–magnitude diagram or intrinsic colors, especially for YSGs, is quite difficult (Drout et al. 2009). Fortunately, M31/M33's kinematics allow us to overcome this problem (Massey et al. 2009, 2016; Drout et al. 2009, 2012). The two galaxies have large negative systemic radial velocities (about $-300\,\mathrm{km\,s^{-1}}$ for M31 and $-200\,\mathrm{km\,s^{-1}}$ for M33) and are both rotating systems. Following Drout et al. (2009, 2012), one can predict the radial velocity (RV) of M31/M33 members according to their positions (X and R):

$$V_{\mathrm{exp}}^{\mathrm{M31}} = -295 + 241.5(X/R), \tag{6}$$

and

$$V_{\mathrm{exp}}^{\mathrm{M33}} = -182 - 81.9(X/R), \tag{7}$$

where X is the distance along M31/M33's semimajor axis, and R is the radial distance of the object within the plane of M31/M33 (Drout et al. 2009, 2012). By comparing the expected RVs, V_{exp}, to the observed ones, the M31/M33 members can be well selected out from the contaminations.

3.1. Observed Radial Velocities from LAMOST LRS

In this study, 3936 spectra of a total of 3280 supergiant candidates in M31 and 1580 ones in M33 have been obtained from the LAMOST DR10 LRS. For sources with multiple observations, we take the one with the highest SNR. The RV measurements, as well as the stellar atmospheric parameters, are derived by the LAMOST stellar parameter pipeline (LASP; Luo et al. 2015). Through comparisons with RV measurements obtained from high-resolution spectroscopy and RV standard stars (Gao et al. 2015; Luo et al. 2015; Huang et al. 2018; Li et al. 2023), the zero offset of LAMOST LRS RV is found to be around $-5\,\mathrm{km\,s^{-1}}$, and the typical precision is also around $-5\,\mathrm{km\,s^{-1}}$. As an independent check, the LAMOST LRS RVs are compared to those derived from MMT spectra by Massey's group (Drout et al. 2009; Massey et al. 2009). Overall, they exhibit excellent consistency, with no significant trends detected along both SNR and stellar color $B-V$ (see Figure 2). The scatter is only $6.79\,\mathrm{km\,s^{-1}}$ for stars with $\mathrm{SNR} > 10$ and $11.46\,\mathrm{km\,s^{-1}}$ even at $5 < \mathrm{SNR} < 10$. The overall median offset is $-5.46\,\mathrm{km\,s^{-1}}$, having excellent consistency with that found by aforementioned studies. An offset of $5\,\mathrm{km\,s^{-1}}$ was therefore added to RVs derived from LAMOST LRS spectra.

3.2. Identifying Supergiants

Now armed with the observed RVs of our supergiant candidates, foreground contaminations could be eliminated by comparing expected RVs predicted from Equations (6) and (7) to the observed ones. In the left panel of Figure 3, two branches are clearly visible: the one with a nearly constant value of zero represents the member stars of M31, while the significant diagonal branch indicates the foreground field stars of the Milky Way. We note the two branches gradually overlap each other with increasing X. This suggests that candidates found in the northeastern corner may still suffer moderate contaminations from the foreground stars. A linear fit was performed for the diagonal branch (represented by the middle solid blue line in the left panel of Figure 3), and a Gaussian function was applied to the fitting residuals to determine their scatter σ; 210 objects falling below the diagonal branch (represented by the best-fit) minus 3σ are considered as M31 supergiant candidates. Among them, 185 were selected from LGGS or Magnier et al. (1992) and 25 were selected from Gaia DR3 photometry; 39 of these 210 candidates have been observed at least two times by LAMOST with $\mathrm{SNR} > 5$. For these, we compare the RV values from different observations and remove four candidates with variation (defined as the difference between maximum and minimum) larger than $50\,\mathrm{km\,s^{-1}}$. This number (4/39) also indicates that the foreground contamination among the M31 supergiant candidates identified with only one observation is no more than 10%. The spectra of the remaining 206 candidates are then visually inspected and seven of them are discarded due to their bad qualities.

In principle, astrometric measurements from Gaia provide another way to distinguish supergiant members of M31 from foreground field stars. Doing so, the numerous RSG candidates of M31 identified by Massey et al. (2021) based on near-infrared (NIR) colors, as well as the Gaia DR2 astrometry, are utilized as a comparison sample. This comparison sample provided a reference for the distribution of parallax and proper motions of young disk-like objects (similar to those in this study) in M31. In total, nearly 4500 RSG candidates in M31 are found with astrometric information from Gaia DR3, with an average parallax of 0.06 ± 0.74 mas, and mean proper motions in R.A. and decl. of -0.15 ± 1.19 and $0.03 \pm 1.36\,\mathrm{mas\,yr^{-1}}$, respectively. Following a similar methodology in Massey et al. (2021), we identify foreground stars among the photometrically selected supergiant candidates (see Tables 1 and 2), with parallax or proper motions falling outside the region that contains 99.5% of the comparison sample. As clearly shown in Figure 4, the foreground stars defined this way are distributed largely (97.5%) in the diagonal branch of the RV differences diagram, with only a few falling below the diagonal branch minus 3σ. A similar case is found for M33. This result confirms the effectiveness of the RV measurements on separating M31/M33 members from foreground contaminations.

Therefore, we combine both RV and Gaia astrometry criteria to select supergiant members. Candidates exhibiting RV differences below the diagonal branch minus 3σ, along with parallax and proper motions within the region containing 99.5% of the comparison sample, are classified as "Rank1" candidates. These candidates have successfully passed through two independent selection criteria, indicating a high level of credibility as true

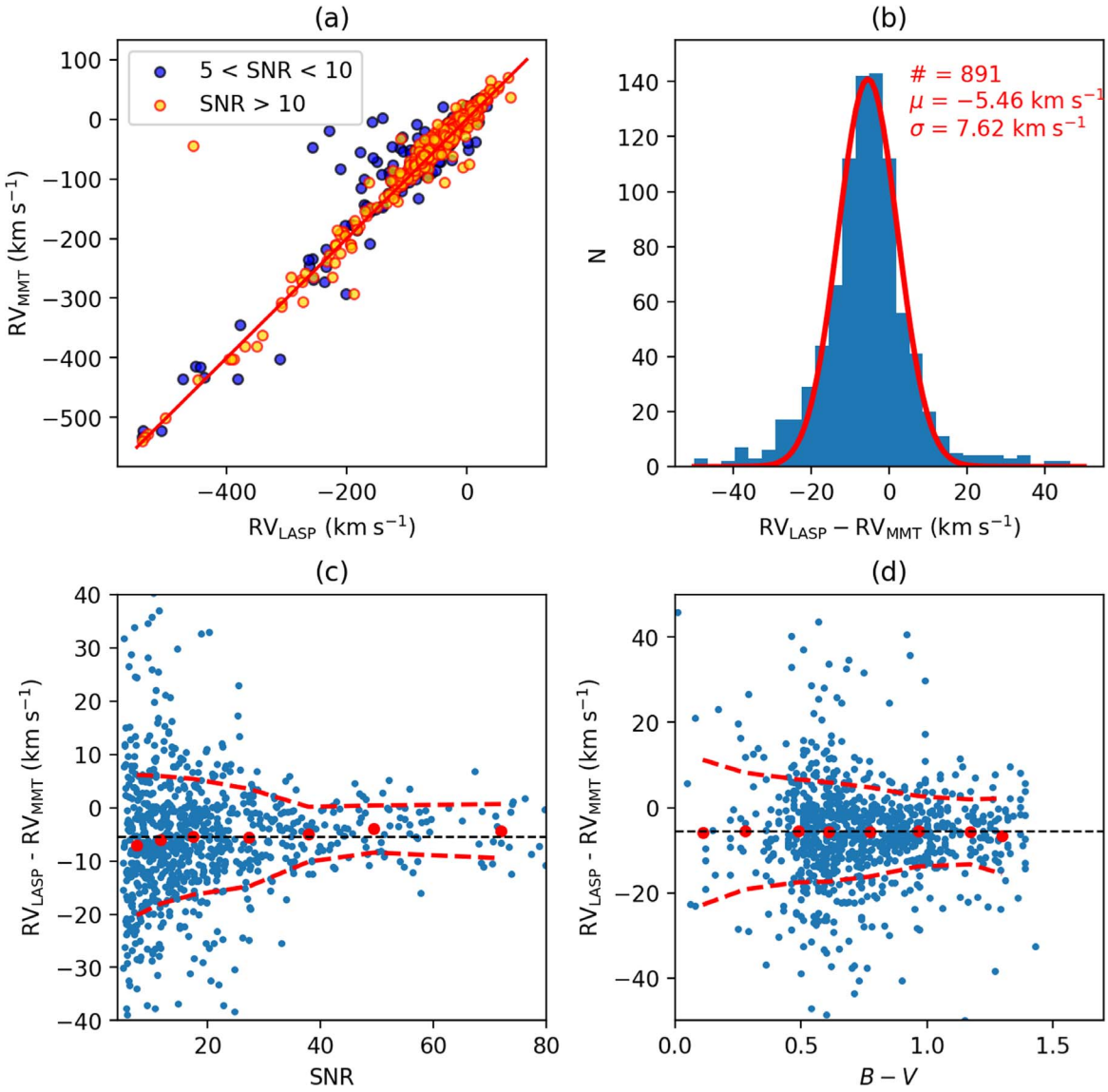

Figure 2. Comparison between observed RVs of 891 objects derived from LASP and MMT. Panel (a) shows the distribution of observed RVs, with the red line indicating the 1:1 line. In panel (b), the histogram illustrates the differences between LASP and MMT observed RVs, with the red line representing a Gaussian fit. Median and standard deviation from the Gaussian fit are also marked in the top-left corner. Panels (c) and (d) show the RV differences in relation to SNR and $B-V$ color, respectively, with the black dashed line representing the median difference. The red dots in panels (c) and (d) represent the mean difference value of each SNR and $B-V$ bin respectively, with the red dashed lines indicating the corresponding 1σ region.

supergiant members of M31/M33. On the other hand, candidates with RV distributions similar to those of "Rank1" candidates, but exhibiting a significant deviation of parallax or proper motions from the mean values of the comparison sample, are classified as "Rank2" candidates. In total, there are 168 "Rank1" and 31 "Rank2" supergiant candidates in M31, represented as blue dots and red diamonds in the left panel of Figure 3, respectively.

Employing the same methodology as M31, we conducted a selection of supergiant candidates of M33. We began by comparing the observed and expected RVs of the photometrically selected supergiant candidates of M33, deriving the best linear regression for objects within the diagonal line and the corresponding scatter σ, as shown in the right panel of Figure 3; 85 objects falling below the diagonal branch minus 3σ were selected as M33 supergiant candidates. Of the 85 candidates, 17 were observed more than once by LAMOST with SNR >5, and none of them show RV variation larger than 50 km s^{-1}. Then after a visual inspection of their spectra, one candidate is excluded due to poor quality. Subsequently, we utilized approximately 2100 M33 RSG candidates from Massey et al. (2021) with available Gaia DR3 astrometric measurements as a comparison sample to double-check

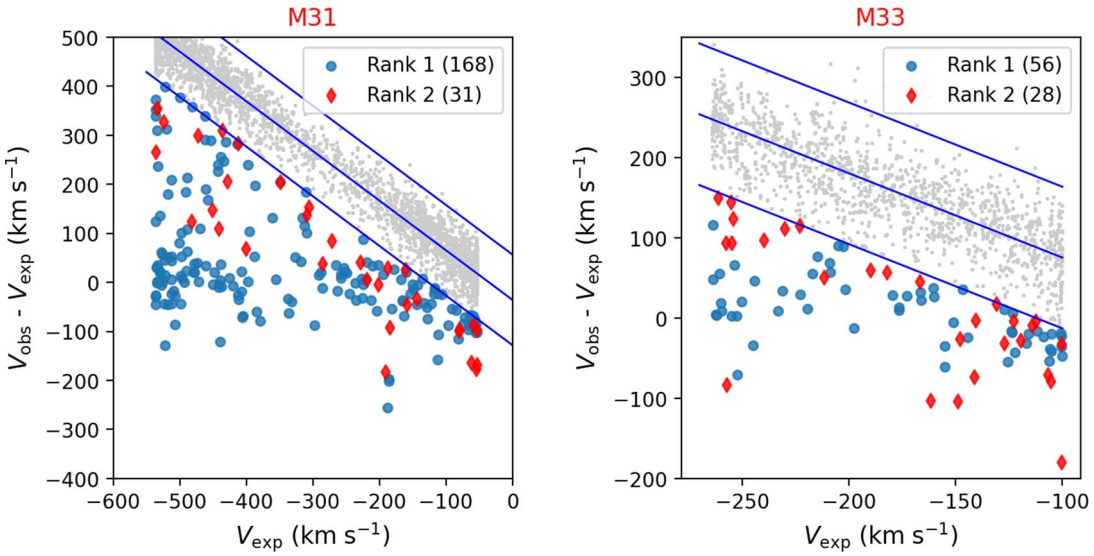

Figure 3. RV distributions of M31 (left) and M33 (right) supergiant candidates. The blue lines represent a linear fit to the diagonal branch, along with the $\pm 3\sigma$ confidence region. Candidates that passed both the RV and Gaia astrometry selections are labeled as "Rank1" (blue dots), while those that only passed RV screening are designated as "Rank2" (red diamonds).

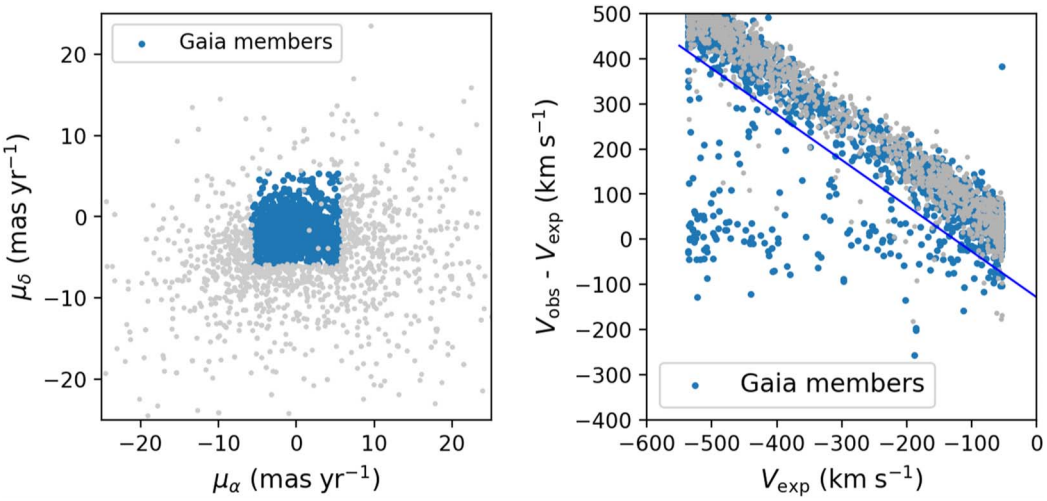

Figure 4. Left: Proper motions of M31 supergiant candidates. The gray dots represent those foregrounds defined by using Gaia astrometry selection, with parallaxes or proper motions falling outside the region that contains 99.5% of the comparison sample. M31 members defined this way are signified as blue dots. Right: RV distribution of M31 supergiant candidates selected astrometrically. Foregrounds defined by using Gaia astrometry selection are signified as gray dots. The blue line represents the area minus 3σ away from the diagonal branch.

foreground contaminations. Following the same procedure used for M31, we identified 56 "Rank1" and 28 "Rank2" M33 supergiant candidates. These are represented by blue dots and red diamonds, respectively, in the right panel of Figure 3.

3.3. Membership Properties and Re-examination

In Figures 5 and 6, the RV and spatial distribution, as well as the color–magnitude diagram, of different types of supergiant candidates in M31/M33 are presented. Note that the color–magnitude diagram in the right panel does not contain candidates without B and V photometry. In the left panel, it is evident that that majority of BSGs and RSGs are located near the region where RV differences are approximately zero, indicating excellent agreement between the observed RVs and the predicted RVs. In contrast, a fraction of YSGs' observed RVs deviate from the predicted ones. Additionally, YSG candidates are more widely distributed in the disk of M31/M33 compared to BSGs and RSGs. Furthermore, in the color–magnitude diagrams, the bluest YSGs in both M31 and M33 extend into the BSG region. This extension is consistent with our loosening of the original color selection to include stars as blue as $B - V = 0$, similar to the criteria set by Drout et al. (2009).

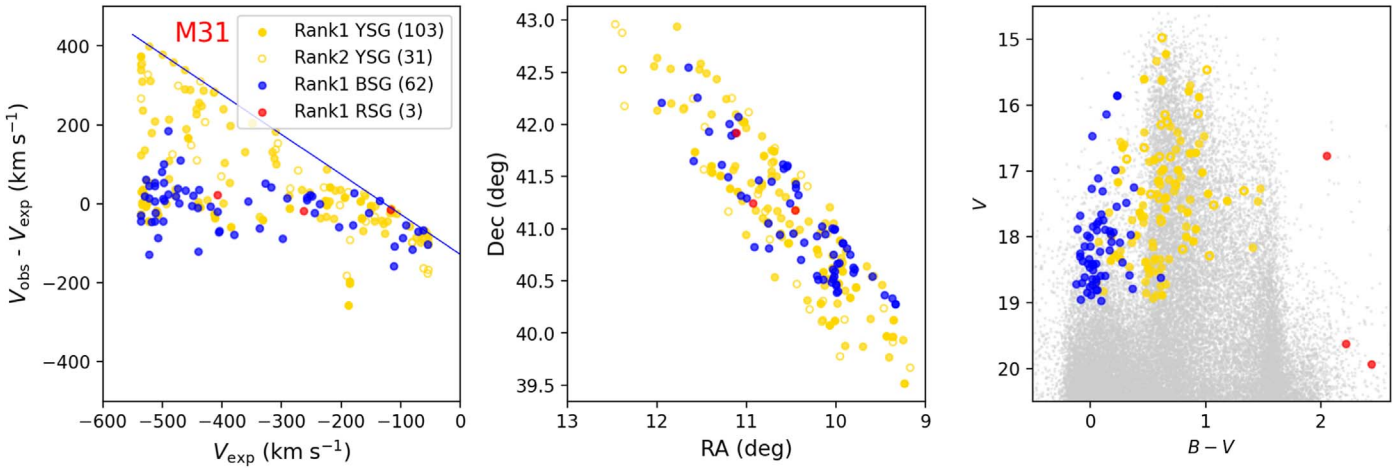

Figure 5. Left panel: The RV distribution of different types of supergiant candidates in M31. "Rank1" YSG, BSG, and RSG candidates are represented by yellow, blue, and red solid circles respectively, while "Rank2" YSG candidates are marked as open yellow circles. Middle panel: The spatial distribution of different types of supergiant candidates in M31. Right panel: The color–magnitude $B - V$ vs. V diagram of different types of supergiant candidates in M31. Background gray dots represent the LGGS objects in the M31 sky region.

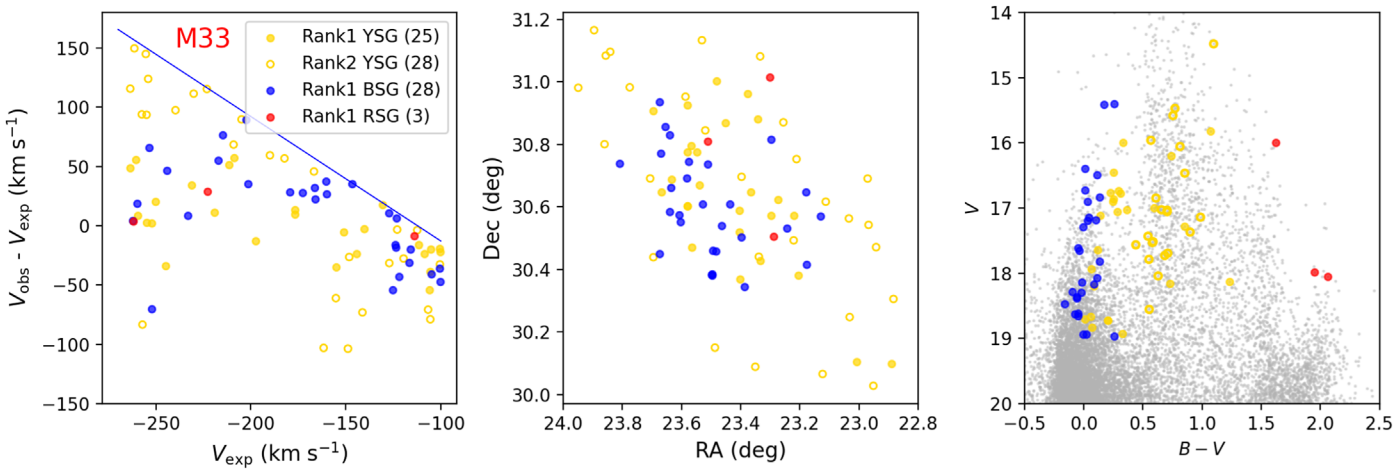

Figure 6. Similar to Figure 5, but for M33 supergiant candidates.

Considering that the RVs of quite a lot of YSG candidates deviate from the predicted values, it is essential to re-examine the spectra of those YSGs, so as to validate their membership in M31. The presence of the O I λ7774 triplet serves as a robust indicator for identifying YSGs. The O I λ7774 triplet is known for its strong luminosity effect in F-type supergiants due to non-local thermodynamic equilibrium (non-LTE) effects (Osmer 1972). The strengths of O I λ7774 can be accentuated by spherical mass outflows of typical supergiants (Przybilla et al. 2000). Candidates exhibiting this feature are considered firm YSGs (Drout et al. 2009). Unfortunately, this feature is hard to be detected in LAMOST spectra due to low SNR and sky emission subtraction issues. Finally, only nine spectra of YSGs show significant O I λ7774 absorption lines. In the future, follow-up high-quality spectroscopy is required to confirm the memberships of those YSG candidates, especially those not sitting around the zero line region (observed minus predicted ones in the RV distribution diagram).

3.4. Comparison with Previous Studies

As mentioned in Section 1, Massey's group has conducted a series of studies to identify supergiant members. Therefore, we cross-matched our candidates with the catalogs published from Massey et al. (2016) and Massey et al. (2021). In total,

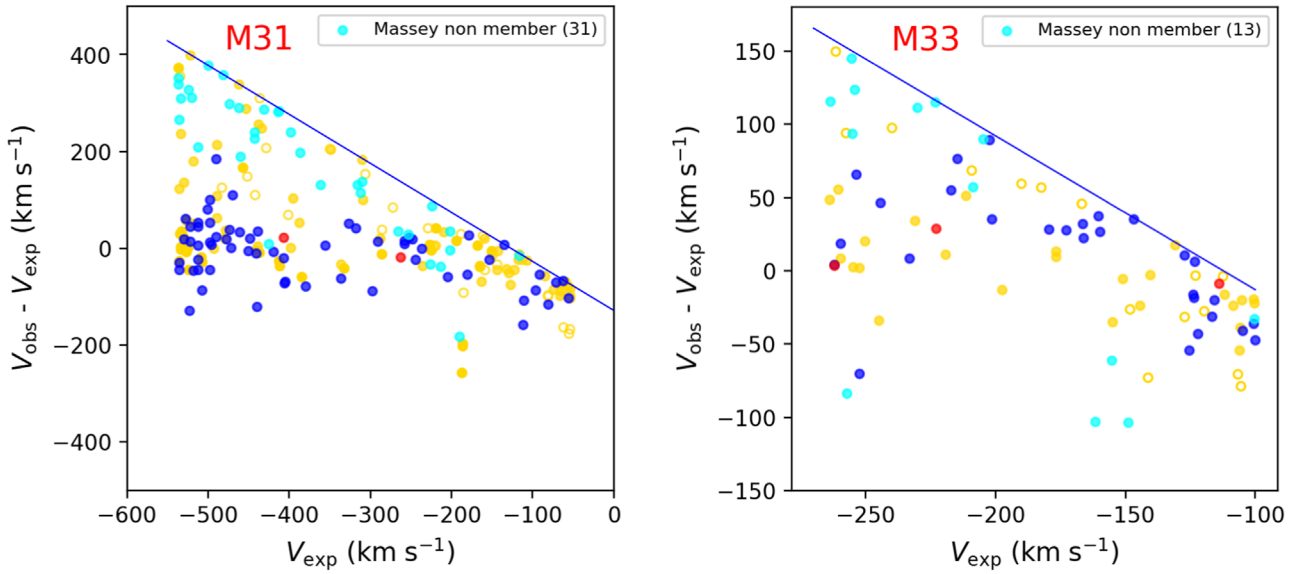

Figure 7. Similar to the left panels of Figures 5 and 6, but with "Massey non-members" marked as cyan dots. The left panel is for M31 and the right panel is for M33.

we found that among the 168 "Rank1" candidates of M31, 87 candidates had been studied by Massey's group and were already in the catalog from Massey et al. (2016), with additional two RSG candidates included in the catalog by Massey et al. (2021) through NIR photometry. Among those 87 candidates, 63 were identified as members, possible members, or unknown, while the other 24 objects were classified as foregrounds by Massey et al. (2016). These 63 candidates, together with the two RSG candidates identified through NIR, are referred to as "Massey members." On the other hand, for those 24 objects classified as foregrounds by Massey et al. (2016), we designate them as "Massey non-members." Additionally, six "Massey members" and seven "Massey non-members" are found among our 31 "Rank2" M31 supergiant candidates. For M33, the 56 "Rank1" supergiant candidates include 36 "Massey members" and one "Massey non-member." Among the 28 "Rank2" candidates of M33, there are five "Massey members" and 12 "Massey non-members." We note that most of these "Massey non-members" are YSGs.

We checked the RV distribution of those "Massey non-members" in Figure 7. The RV differences of most of them are very close to the diagonal branch minus 3σ. Considering that none of them are confirmed with the O I λ7774 triplet, their memberships in M31/M33 are required to be explored by further observations as suggested earlier.

4. Results and Discussion

We present the supergiant candidates identified in this work in Tables A1 and A2. A more detailed version of the catalogs, including R.A., decl., and LAMOST observation times with SNR >5, is available in electronic form in the online version of this manuscript.[8]

4.1. Physical Properties and HR-Diagram

In order to examine the distribution of our supergiant candidates of M31/M33 within the H-R diagram and check their consistency with current stellar evolutionary tracks, it is essential to derive their effective temperatures and bolometric luminosities.

For candidates with B and V photometry available in M31, we apply a constant reddening correction of $E(B-V)=0.13$. This is the median value found for early-type stars in M31 by Massey et al. (2007) and is widely employed in the analysis of M31's supergiants. For stars with Gaia photometry, the reddening coefficient is then taken from Huang et al. (2021). As our candidates, mostly BSGs and YSGs, cover a wide range of dereddened colors $(B-V)_0$ from -0.25 to 2.31, they span a wide range of effective temperatures. Drout et al. (2009) provided transformations using the "Atlas9" model (Kurucz 1992) for objects with $0.03 \leqslant (B-V)_0 \leqslant 1.26$. A significant fraction of our candidates fall outside this range. Consequently, we opt to employ data from the YBC database (Chen et al. 2019) to derive effective temperature–color relations and bolometric correction (BC) with a wide application range of color. The BC values in different temperature ranges in the YBC database are the optimized results provided after comparing the results derived from various models (more details are in Chen et al. 2019). Additionally, the YBC database allows the choosing of different stellar masses and metallicities. By restricting the initial mass within the typical range for supergiants and fixing the metallicity as $2\,Z_{\odot}$, we obtain the

[8] The online version has been published at https://www.scidb.cn/en/s/F3Yn2q.

corresponding transformation from dereddened colors $(B-V)_0$ to effective temperatures, encompassing a broader color range $-0.37 \leqslant (B-V)_0 \leqslant 1.53$, as well as the BCs. Note that three RSGs are not included in the transforming process due to their extremely high $B-V$ values, and therefore are not included in the H-R diagram below.

The relationship between $(B-V)_0$ and $\log T_{\rm eff}$ for supergiant candidates in M31 is as follows:

$$\log T_{\rm eff} = \begin{cases} 3.94 - 0.8644(B-V)_0 + 4.424(B-V)_0^2, & (B-V)_0 \leqslant 0.03, \\ 3.924 - 0.3812(B-V)_0 + 0.3607(B-V)_0^2 - 0.1722(B-V)_0^3, & (B-V)_0 > 0.03. \end{cases} \tag{8}$$

The corresponding BCs are as follows:

$$\mathrm{BC} = \begin{cases} -221.1 + 114.8\log T_{\rm eff} - 14.89(\log T_{\rm eff})^2, & \log T_{\rm eff} \leqslant 4.1, \\ 21.98 - 5.544\log T_{\rm eff}, & \log T_{\rm eff} > 4.1. \end{cases} \tag{9}$$

For candidates with only available Gaia photometry, we establish similar transformation from $(G_{\rm BP}-G_{\rm RP})_0$ to $\log T_{\rm eff}$ and the corresponding BC values for $(G_{\rm BP}-G_{\rm RP})_0$ ranging from -0.1 to 1.24, based on data from the YBC database:

$$\begin{aligned} \log T_{\rm eff} &= 3.953 - 0.3905(G_{\rm BP}-G_{\rm RP})_0 \\ &\quad + 0.3081(G_{\rm BP}-G_{\rm RP})_0^2 \\ &\quad - 0.1263(G_{\rm BP}-G_{\rm RP})_0^3, \\ \mathrm{BC} &= -179.4 + 93.89\log T_{\rm eff} - 12.27(\log T_{\rm eff})^2. \end{aligned} \tag{10}$$

For M33 candidates, we apply a constant reddening correction of $E(B-V)=0.12$, and compute the transformation relationship based on the YBC database. We set the metallicity as 0.6 $Z_\odot$, in line with Drout et al. (2012). For candidates with B and V photometry available, the relationship between $(B-V)_0$ and $\log T_{\rm eff}$ is as follows:

$$\log T_{\rm eff} = \begin{cases} 3.942 - 1.159(B-V)_0 + 5.187(B-V)_0^2 + 8.167(B-V)_0^3, & (B-V)_0 \leqslant 0.06, \\ 3.907 - 0.318(B-V)_0 + 0.1899(B-V)_0^2 - 0.06115(B-V)_0^3, & (B-V)_0 > 0.06. \end{cases} \tag{11}$$

The BCs are as follows:

$$\mathrm{BC} = \begin{cases} -268.4 + 139.6\log T_{\rm eff} - 18.15(\log T_{\rm eff})^2, & \log T_{\rm eff} \leqslant 4.0, \\ 3.419 + 6.296\log T_{\rm eff} - 1.378(\log T_{\rm eff})^2, & \log T_{\rm eff} > 4.0. \end{cases} \tag{12}$$

For candidates of M33 selected based on Gaia, the transformation and BC for objects with $(G_{\rm BP}-G_{\rm RP})_0$ ranging from 0.2 to 1.4 are as follows:

$$\begin{aligned} \log T_{\rm eff} &= 3.933 - 0.3107(G_{\rm BP}-G_{\rm RP})_0 \\ &\quad + 0.1895(G_{\rm BP}-G_{\rm RP})_0^2 - 0.08074(G_{\rm BP}-G_{\rm RP})_0^3, \\ \mathrm{BC} &= -162.2 + 84.91\log T_{\rm eff} - 11.1(\log T_{\rm eff})^2. \end{aligned} \tag{13}$$

Applying distance modulus of 24.40 and 24.60 for M31 and M33, respectively, as taken from van den Bergh (2000), we derive the bolometric luminosities of all M31/M33's "Rank1" and "Rank2" supergiants.

In Figure 8, we present the locations of supergiant candidates of M31/M33 in the H-R diagram. Geneva evolutionary tracks for 2 and 0.6 $Z_\odot$, with an initial rotation speed of 40% of the breakup speed, are overplotted (Yusof et al. 2022; Eggenberger et al. 2021). Notably, in the left panel of Figure 8, there are four "Rank2" YSG candidates of M31 with extremely high luminosities, inconsistent with the evolutionary tracks. A similar scenario is observed in the right panel of Figure 8, where the most luminous four "Rank2" YSGs deviate from the evolutionary tracks. Considering their "Rank2" properties, without the O I λ7774 triplet confirmed in their spectra, we doubt their status as genuine YSGs, and further confirmation is required. The locations of other supergiant candidates exhibit an excellent agreement with the evolutionary tracks.

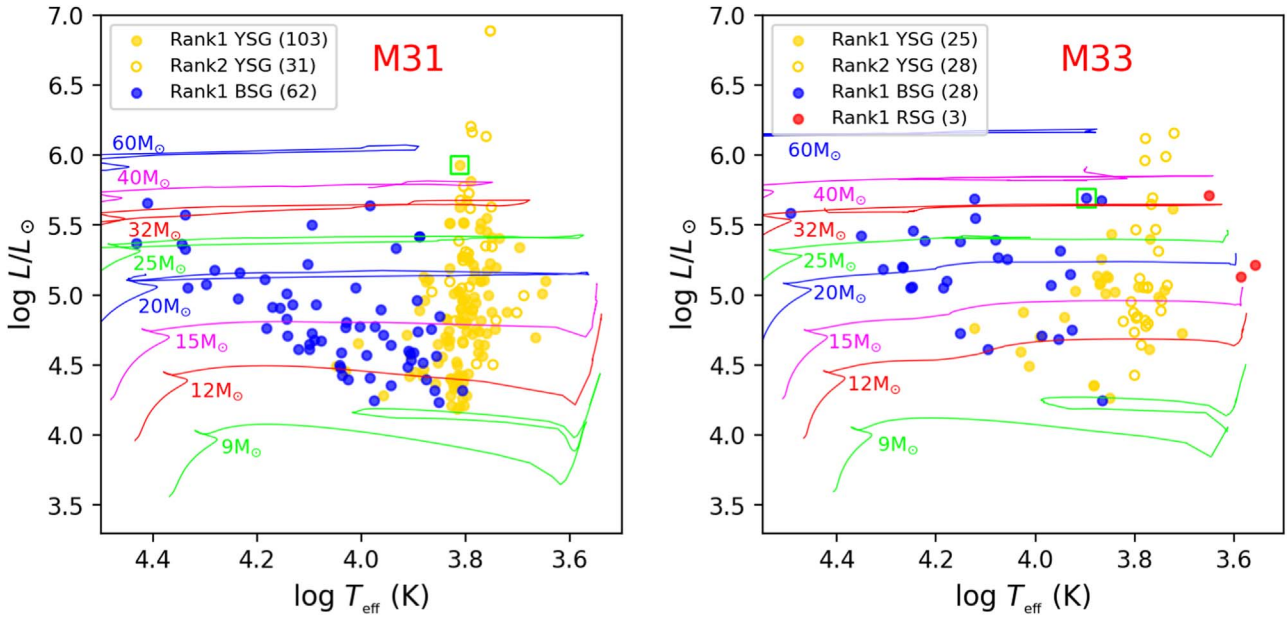

Figure 8. H-R diagrams for "Rank1" and "Rank2" supergiant candidates of M31 (left) and M33 (right). The overplotted lines with different colors show the Geneva evolutionary tracks for 2 times solar metallicity for M31 and 0.6 times solar metallicity for M33, with an initial rotation speed of 40% of the breakup speed. The green boxes enclose the most massive "Rank1" candidates of M31 and M33.

Among our "Rank1" candidates of M31, the most massive one is LAMOST J0043+4124, highlighted by a green box in the left panel of Figure 8, with a mass of over 40 $M_{\odot}$. This object has the brightest apparent G magnitude among our "Rank 1" candidates and is located in the region with expected RVs greater than $-100\,\mathrm{km\,s^{-1}}$. In this region, the M31 members and the foregrounds may not be well separated by RVs (Hartmann & Burton 1997). However, considering that it passes both the RV and Gaia astrometry criteria successfully, we have chosen to retain it as a YSG candidate. In the case of M33, the most massive one among the new "Rank1" candidates is a BSG, J0134+3044. Highlighted by a green box in the right panel of Figure 8, it is estimated to be more than $\sim$32 $M_{\odot}$ based on evolutionary tracks, and this object has been analyzed by Liu et al. (2022) through spectroscopic methods. The effective temperature and bolometric luminosity derived by Liu et al. (2022) are in agreement with our estimations in this work, indicating the reliability of our newly derived transformation relations.

4.2. Spatial Distribution and Possible Substructures

In Figure 9, we present the spatial distribution of our "Rank1" and "Rank2" supergiant candidates in Herschel SPIRE 250 μm (Fritz et al. 2012) and H I 21 cm (Braun et al. 2009) images of M31. In the left panel, the majority of the supergiant candidates fall along the CO ring, which corresponds to the high star formation region, in line with our expectations. Additionally, several supergiant candidates are found outside the CO ring, including two extended substructures of M31's disk. One is in the southwestern corner, which has already been validated as a part of M31 (Braun et al. 2009; Fritz et al. 2012). This substructure is highlighted by a yellow box in Figure 9, and the LBV found by Huang et al. (2019) is situated in this substructure. The other substructure is located in the northeast corner and includes 11 candidates, highlighted by a white box in Figure 9, commented as "NE" in Table A1. Among these candidates, 10 are YSGs (nine "Rank1" and one "Rank2") and one is a BSG ("Rank1"). In the right panel, these candidates are found near the gas ring. This region faces significant contamination from foreground Galactic emission, suggesting the observed gas may predominantly originate from the Milky Way, not M31 itself. Fritz et al. (2012) analyzed this region using Herschel far-infrared data, correcting for the foreground dust component, but could not conclusively determine whether the substructure belongs to the Galactic foreground or M31. If follow-up observations confirm that the 11 supergiant candidates are members of M31, it would provide strong evidence for the ownership of this substructure. This will be a significant component of our future work.

In the left panel of Figure 10, we present the spatial distribution of our supergiant candidates in Herschel SPIRE 250 μm image of M33. Similar to M31, the majority of supergiant candidates are distributed along the CO ring. Additionally, four YSG candidates (two "Rank1" and two "Rank2") are positioned in the southwestern corner of M33 and commented as "SW" in Table A2. To investigate if there are

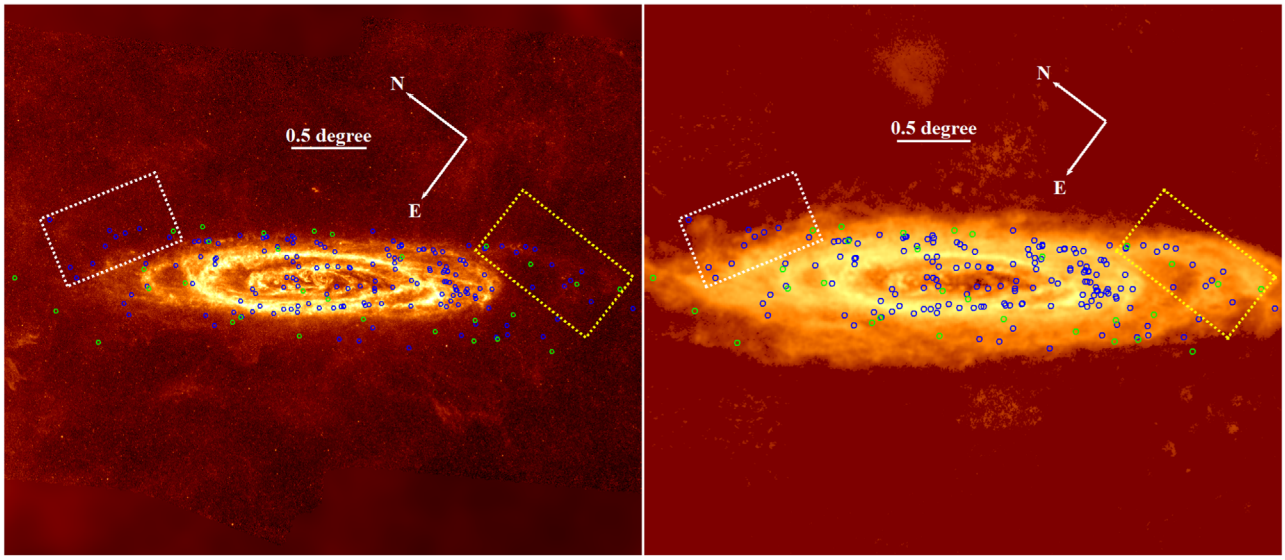

Figure 9. Left: Spatial distribution of supergiant candidates in M31 based on the Herschel SPIRE 250 μm image (Fritz et al. 2012). The blue circles mark the locations of "Rank1" supergiant candidates, while the green circles represent the positions of "Rank2." The white and yellow dashed boxes highlight substructures in the northeastern and southwestern corners, respectively. Spatial scale and compass are shown in the upper part. Right: Spatial distribution of supergiant candidates in M31 based on the H I 21 cm map (Braun et al. 2009).

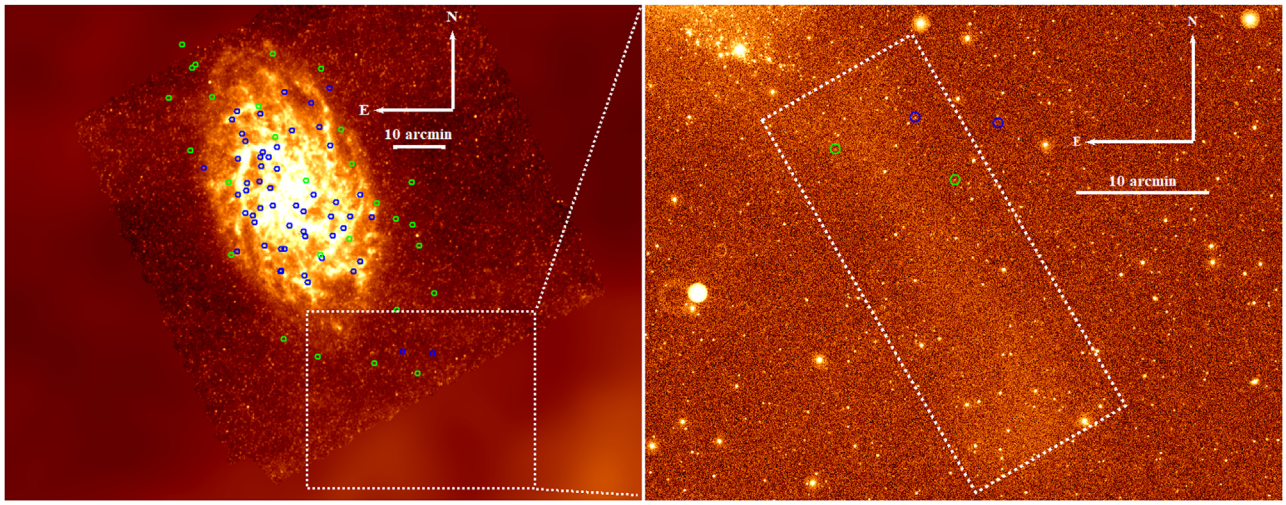

Figure 10. Left: Spatial distribution of supergiant candidates of M33 Herschel SPIRE 250 μm image. The blue circles mark the locations of the "Rank1" supergiant candidates, and the green circles represent those of "Rank2." The spatial scale and compass are displayed in the top-right. Right: Image of the southwestern corner of M33 in GALEX NUV band. The white dashed box highlights an extended substructure from M33's disk, where three supergiant candidates are distributed.

any supporting substructures for these potential supergiant members, we use an image from the GALEX NUV band, as shown in the right panel of Figure 10. An extended substructure originating from M33's disk is visible, marked by a white dashed box. Three YSG candidates are located on the edge of this substructure. As part of our future work, we plan to conduct follow-up observations for these candidates to further analyze this possible substructure.

5. Summary

Based on LAMOST DR10 data, we conducted a systematic identification of supergiant members in M31 and M33. First, objects in M31/M33 from LAMOST DR10 were cross-matched with the LGGS catalog or Gaia DR3 to acquire their photometric data. BSG, YSG, and RSG candidates were then selected based on criteria adopted from previous studies. Subsequently, we

excluded foreground field stars by comparing observed RVs to expected ones, as well as using the Gaia astrometry. In total, we identified 199 supergiant candidates in M31, with 168 "Rank1" and 31 "Rank2." For M33, 84 supergiant candidates, including 56 "Rank1" and 28 "Rank2," were found. Our future work involves conducting follow-up spectroscopy for YSG candidates with low SNR to determine their memberships.

We constructed color-effective temperature and BC relations based on the YBC database to derive the effective temperatures and BCs of the candidates, and examined the distribution of these candidates in the H-R diagrams. Furthermore, we checked the consistency between the locations of supergiant candidates and those expected from the Geneva evolutionary tracks. The results revealed an agreement, especially for "Rank1" candidates.

Upon analyzing the spatial distribution of candidates, we identified a potential substructure in the northeastern corner of M31 and another one in the southwestern corner of M33. The northeastern corner of M31 suffers significant contamination from Galactic emission, posing challenges in determining whether the substructure belongs to M31 or primarily is dominated by foreground emission. The follow-up validation of supergiant candidates within this substructure is crucial. Once confirmed, it would substantially contribute to ascertaining the ownership of the substructure. Likewise, the substructure in the southwestern corner of M33, along with the supergiant candidates within, also requires further analysis. These will be crucial aspects of our future research.

Acknowledgments

This work was funded by the National Natural Science Foundation of China (NSFC, grant Nos. 12090040, 12090044, 12133001, and 12422303), Beijing Natural Science Foundation (no. 1242016) and the science research grants from the China Manned Space Project. This work was partially supported by the Talents Program (24CE-YS-08) and the Popular Science Project (24CD012) of the Beijing Academy of Science and Technology.

This work has made use of data products from the Guo Shou Jing Telescope (the Large Sky Area Multi-Object Fiber Spectroscopic Telescope, LAMOST). LAMOST is a National Major Scientific Project built by the Chinese Academy of Sciences. Funding for the project has been provided by the National Development and Reform Commission. LAMOST is operated and managed by the National Astronomical Observatories, Chinese Academy of Sciences.

Appendix
M31 and M33 Supergiant Candidates

Here we present our supergiant candidates of M31 and M33 identified in this work in Tables A1 and A2. A more detailed version of the catalogs have been published at http://www.scidb.cn/en/s/F3Yn2q.

Table A1
199 Supergiants in M31

Star[a]	V_{obs}	V_{exp}	$V_{obs} - V_{exp}$	V	$B - V$	SNR	Rank	Note[b]	Comment[c]
				Blue Supergiants					
J0037+4016	−450.1	−497.7	47.6	15.854	0.231	25.7	1	⋯	Huang+2019; Liu+2022
J0037+4020	−310.8	−490.6	179.8	17.310	0.107	10.1	1	B1I	⋯
J0037+4021	−546.7	−498.3	−48.3	18.146	−0.002	7.9	1	⋯	⋯
J0038+4032	−462.8	−477.6	14.9	17.763	0.073	6.6	1	B9.5I+	⋯
J0039+4036	−425.1	−501.2	76.1	17.653	0.096	10.5	1	B2.5Ia	⋯
J0039+4034	−561.3	−512.6	−48.7	18.805	0.050	5.1	1	⋯	
J0039+4037	−490.2	−498.2	8.0	18.199	0.167	5.3	1	⋯	⋯
J0039+4045	−431.9	−461.2	29.3	18.701	−0.073	6.8	1	O9.5I	⋯
J0039+4048	−432.3	−488.2	15.8	17.887	0.126	7.6	1	B8I	⋯
J0039+4051	−407.4	−438.5	31.1	18.469	−0.008	8.1	1	B8I	⋯
J0039+4051	−565.8	−439.6	−126.1	18.956	−0.086	5.5	1	B1.5I	⋯
J0039+4040	−656.5	−522.7	−133.7	18.645	0.014	5.4	1	⋯	⋯
J0039+4024	−465.1	−512.8	47.7	18.728	0.014	5.5	1	B8Ia	⋯
J0039+4040	−470.8	−527.7	56.9	18.250	−0.090	11.6	1	B0.5I	⋯
J0039+4023	−598.9	−507.4	−91.5	18.968	0.095	5.3	1	B0.7Ia	⋯
J0039+4028	−513.0	−522.2	9.2	18.338	−0.014	5.5	1	B2.5I	⋯
J0040+4027	−568.2	−518.1	−50.1	18.718	−0.120	6.1	1	⋯	⋯
J0040+4035	−585.5	−535.8	−49.6	18.811	0.058	5.0	1	⋯	⋯
J0040+4059	−478.8	−404.6	−74.1	18.595	0.127	5.8	1	B2.5I	⋯
J0040+4032	−515.3	−523.0	14.7	17.901	0.055	12.5	1	⋯	Liu+2022
J0040+4059	−431.3	−407.2	−24.1	18.643	0.047	5.1	1	⋯	⋯
J0040+4045	−511.7	−512.9	1.2	18.880	0.003	5.4	1	B5I	⋯
J0040+4036	−570.0	−536.0	−34.0	18.756	−0.007	7.0	1	B7I	⋯
J0040+4031	−482.2	−522.5	40.4	18.590	0.089	6.1	1	B1I+Neb	⋯

Table A1
(Continued)

Star[a]	V_{obs}	V_{exp}	$V_{obs} - V_{exp}$	V	$B - V$	SNR	Rank	Note[b]	Comment[c]
J0040+4100	−482.1	−405.9	−76.2	18.583	0.337	5.1	1	⋯	⋯
J0040+4029	−472.9	−512.4	39.5	18.846	−0.026	6.6	1	⋯	⋯
J0040+4056	−459.5	−450.1	−9.4	17.967	0.349	6.5	1	B8I	⋯
J0040+4030	−471.7	−490.3	18.6	17.747	0.111	11.8	1	BI	⋯
J0040+4101	−431.9	−420.0	−11.9	17.933	0.198	9.7	1	⋯	Liu+2022
J0040+4030	−365.1	−469.9	104.8	18.412	0.049	9.5	1	⋯	⋯
J0040+4033	−439.5	−473.8	34.3	16.989	0.216	24.3	1	cLBV	⋯
J0040+4055	−493.9	−496.3	2.4	18.073	0.185	8.9	1	B2.5	⋯
J0041+4052	−539.7	−512.1	−27.6	17.485	0.308	13.9	1	A6I	⋯
J0041+4042	−456.0	−441.2	−14.7	17.841	0.021	10.2	1	⋯	Liu+2022
J0041+4119	−280.8	−317.9	37.1	18.617	0.606	7.3	1	⋯	⋯
J0041+4123	−390.8	−297.8	−93.0	18.403	0.017	5.0	1	⋯	⋯
J0041+4125	−281.7	−290.9	9.2	18.690	0.048	7.9	1	⋯	⋯
J0041+4057	−474.8	−471.8	−2.9	17.910	0.168	11.3	1	B8I	⋯
J0042+4114	−354.6	−355.9	1.3	18.088	0.256	16.3	1	⋯	Liu+2022
J0042+4136	−253.7	−257.9	4.2	17.807	0.056	8.2	1	B6V	⋯
J0042+4135	−246.8	−257.7	10.9	17.541	0.225	11.1	1	B8I	⋯
J0042+4134	−234.9	−252.3	17.4	18.305	−0.088	5.3	1	⋯	⋯
J0042+4137	−235.2	−248.7	13.5	18.506	0.019	5.0	1	⋯	⋯
J0042+4056	−462.8	−379.4	−83.3	18.430	0.026	12.7	1	B2I	⋯
J0042+4127	−267.9	−204.4	−63.4	17.265	0.012	10.4	1	Star+N	⋯
J0042+4048	−962.4	−349.9	−612.5	18.142	−0.048	6.9	1	B1.5I	⋯
J0043+4103	−403.8	−336.3	−67.4	18.386	0.278	6.2	1	B2I	⋯
J0043+4128	−134.4	−62.8	−71.6	18.616	−0.049	10.3	1	⋯	⋯
J0043+4049	−280.9	−327.0	46.1	18.012	−0.008	6.4	1	⋯	⋯
J0044+4117	−272.8	−244.4	−28.4	18.788	0.367	11.6	1	⋯	⋯
J0044+4119	−242.2	−236.6	−5.7	18.365	−0.067	9.6	1	⋯	⋯
J0044+4204	−182.6	−153.8	−28.7	16.465	0.017	14.1	1	B0.5I	⋯
J0044+4155	−275.5	−112.2	−163.3	17.680	−0.088	7.0	1	B1.5Ia	⋯
J0044+4153	−149.9	−91.5	−58.4	17.253	0.377	9.8	1	B8Ia	⋯
J0044+4200	−222.7	−111.0	−111.7	17.878	−0.113	6.7	1	⋯	⋯
J0044+4129	−156.7	−178.5	21.8	17.982	−0.027	12.3	1	B0.7Ib	⋯
J0045+4136	−132.8	−135.2	2.4	17.962	0.177	9.8	1	B8V	⋯
J0045+4156	−162.9	−55.2	−107.6	17.108	0.068	15.4	1	B2.5I	⋯
J0046+4215	−147.2	−71.3	−75.8	18.218	−0.083	6.0	1	⋯	⋯
J0046+4138	−239.9	−180.9	−59.0	16.140	0.137	22.1	1	B8Ie	⋯
LAMOST J0046+4232	−188.6	−96.7	−91.9	⋯	⋯	17.6	1	⋯	NE
J0047+4212	−201.7	−81.0	−120.7	18.411	−0.021	5.2	1	⋯	⋯
				Yellow Supergiants					
LAMOST J0036+3940	−184.2	−534.3	350.1	⋯	⋯	7.9	2	⋯	⋯
LAMOST J0036+3931	−471.9	−518.4	46.5	⋯	⋯	14.5	1	⋯	⋯
LAMOST J0036+3956	−510.2	−534.2	24.0	⋯	⋯	8.9	1	⋯	⋯
J0037+4007	−474.1	−526.6	52.5	18.474	0.496	5.7	1	YSG:	⋯
J0037+3954	−274.3	−535.8	261.4	16.789	0.695	15.2	2	fgd	⋯
J0037+3957	−171.1	−528.0	356.9	17.755	0.438	5.6	1	fgd	⋯
LAMOST J0037+3946	−127.6	−521.9	394.3	⋯	⋯	6.7	1	⋯	⋯
J0037+3958	−509.0	−535.0	26.0	17.160	0.594	6.3	1	F5Ia	⋯
J0037+4014	−202.2	−524.2	322.0	16.135	0.935	33.2	2	fgd	⋯
LAMOST J0037+4027	−464.3	−479.5	15.2	⋯	⋯	11.5	1	⋯	Weak 7774?
J0038+4032	−179.3	−473.3	294.0	16.255	0.666	19.4	2	fgd	⋯
J0038+4032	−445.3	−478.1	32.8	17.459	1.453	7.6	1	⋯	⋯
J0038+4008	−228.8	−533.8	305.0	16.324	0.692	6.9	1	fgd	⋯
J0038+4038	−128.3	−462.1	333.8	15.696	0.862	15.5	1	⋯	⋯
J0038+3952	−431.3	−489.1	57.7	18.689	0.055	9.1	1	⋯	⋯
J0039+4026	−540.5	−534.1	−6.4	16.735	0.862	9.7	1	G0Ia	⋯
J0039+4020	−511.8	−529.4	17.7	18.357	0.176	6.1	1	A0I	⋯
J0039+4047	−276.2	−460.6	184.3	17.213	0.603	14.6	1	fgd	⋯
J0039+4024	−398.6	−529.8	131.2	18.562	0.511	5.6	1	⋯	⋯
LAMOST J0039+3952	−169.4	−453.5	284.0	⋯	⋯	10.8	1	⋯	⋯

Table A1
(Continued)

Star[a]	V_{obs}	V_{exp}	$V_{obs} - V_{exp}$	V	$B - V$	SNR	Rank	Note[b]	Comment[c]
J0039+4007	−362.8	−482.8	120.0	18.191	0.801	5.1	2	YSG:	⋯
J0039+4040	−308.6	−512.3	203.7	18.151	0.542	15.2	1	fgd	⋯
J0039+4051	−440.2	−439.3	−0.9	17.267	1.471	7.7	1	⋯	⋯
J0039+4035	−502.1	−532.9	30.8	17.170	0.235	19.1	1	YSG	7774
J0039+4043	−127.0	−499.6	327.4	17.842	0.829	5.8	1	fgd	⋯
J0039+4038	−528.9	−525.4	−3.4	17.884	0.915	7.0	1	G8I	⋯
J0039+4038	−523.6	−526.7	3.0	17.401	0.653	9.3	1	F8I	⋯
LAMOST J0039+3946	−131.2	−436.1	304.9	⋯	⋯	11.4	2	⋯	⋯
J0039+4053	−450.7	−436.8	−13.9	17.344	1.020	13.4	1	G4Ie	⋯
J0039+4028	−538.5	−527.3	−11.1	17.451	1.184	5.7	1	YSG	⋯
J0039+4016	−280.1	−488.8	208.7	18.683	0.476	6.0	1	⋯	⋯
J0040+4006	−294.8	−457.4	162.6	17.976	0.398	7.4	1	YSG:	⋯
J0040+4103	−194.1	−386.2	192.1	18.083	0.536	12.3	1	fgd	⋯
J0040+4031	−572.8	−523.8	−49.0	17.628	0.840	7.8	1	YSG	⋯
J0040+4037	−567.1	−536.0	−31.1	18.272	0.203	8.3	1	A8I	⋯
J0040+4044	−212.7	−519.8	307.2	17.012	0.608	13.3	1	fgd	⋯
J0040+4004	−449.6	−440.7	−8.9	18.334	0.256	5.4	1	YSG	⋯
LAMOST J0040+4112	−148.9	−348.8	200.0	⋯	⋯	6.6	1	⋯	⋯
J0040+4031	−532.0	−509.0	−23.0	16.648	0.275	16.2	1	F0Ia	7774
J0040+4056	−337.1	−441.9	104.8	16.823	0.316	5.6	2	⋯	⋯
J0040+4103	−163.3	−397.9	234.6	18.089	0.361	10.7	1	fgd	⋯
J0040+4027	−128.0	−481.5	353.5	16.860	0.509	6.1	1	fgd	⋯
J0040+4035	−540.6	−507.5	−33.0	17.701	0.440	10.8	1	F8I	⋯
J0040+4058	−187.0	−438.4	251.3	18.517	0.537	7.8	1	⋯	⋯
J0040+4018	−308.5	−451.5	143.0	16.299	0.614	17.1	2	YSG:	⋯
J0040+4007	−149.4	−431.2	281.9	16.467	0.988	12.8	1	fgd	⋯
J0040+4006	−226.4	−428.2	201.8	17.768	0.614	5.3	2	⋯	⋯
J0040+4017	−208.4	−443.0	234.6	17.306	0.436	15.1	1	fgd	⋯
J0040+4057	−175.9	−462.0	286.1	17.344	0.573	9.1	1	fgd	⋯
J0040+4045	−300.9	−533.4	232.4	16.554	0.258	8.6	1	⋯	⋯
J0040+4048	−168.5	−536.3	367.8	18.884	0.619	9.5	1	⋯	⋯
J0041+4013	−133.5	−412.5	279.0	17.520	1.070	7.0	2	fgd	⋯
J0041+4104	−192.0	−434.4	242.4	18.543	0.587	13.5	1	⋯	⋯
LAMOST J0041+4124	−157.9	−306.0	148.1	⋯	⋯	21.6	2	⋯	⋯
J0041+4018	−136.7	−413.7	277.0	17.566	0.786	7.8	1	fgd	⋯
LAMOST J0041+4130	−252.1	−285.4	33.3	⋯	⋯	12.4	2	⋯	⋯
Mag J0041+4059	−417.2	−535.7	118.6	15.630	0.620	5.4	1	⋯	⋯
J0041+4028	−337.2	−401.1	63.9	18.291	1.033	15.7	2	YSG	⋯
J0041+4111	−296.6	−395.8	99.1	18.465	0.615	9.3	1	⋯	⋯
J0041+4127	−303.2	−286.0	−17.2	17.994	0.829	9.3	1	YSG	⋯
J0041+4057	−385.7	−489.2	103.5	18.163	1.409	6.7	1	⋯	⋯
J0042+4102	−498.1	−493.1	−5.0	18.829	0.112	9.2	1	⋯	⋯
J0042+4051	−444.4	−412.9	−31.6	17.025	0.966	8.0	1	G5Ia	⋯
J0042+4051	−452.5	−411.9	−40.6	16.988	0.761	5.6	1	F5Ia	⋯
J0042+4118	−202.2	−312.3	110.1	17.133	0.682	12.8	1	fgd	⋯
J0042+4055	−339.4	−387.7	48.3	18.885	0.571	6.1	1	⋯	⋯
J0042+4106	−420.7	−425.0	4.3	16.413	0.750	5.0	1	fgd	⋯
J0042+4057	−448.9	−384.7	−64.2	17.628	0.425	13.4	1	A4I	⋯
J0042+4121	−235.1	−265.7	−30.6	17.431	0.864	9.7	1	fgd	⋯
J0042+4110	−400.8	−397.9	−2.9	18.929	0.543	19.5	1	⋯	⋯
J0042+4129	−276.0	−235.3	−40.7	18.209	0.259	10.1	1	⋯	⋯
J0042+4146	−192.5	−228.8	36.3	17.201	0.739	6.6	2	YSG:	⋯
J0042+4032	−235.2	−361.4	126.2	17.788	0.459	8.8	1	fgd	⋯
J0042+4144	−223.8	−226.8	3.0	17.985	0.181	5.5	1	A7I	⋯
J0042+4144	−262.7	−225.7	−37.0	16.410	0.465	5.6	1	fgd	⋯
J0042+4138	−141.7	−224.1	82.4	17.720	0.602	8.9	1	fgd	⋯
J0042+4137	−218.9	−219.2	0.3	14.975	0.621	35.8	2	YSG:	⋯
J0042+4145	−222.1	−220.9	−1.2	17.632	0.161	5.2	1	⋯	⋯
J0042+4130	−181.3	−210.0	28.7	18.753	0.606	5.6	1	⋯	⋯

Table A1
(Continued)

Star[a]	V_{obs}	V_{exp}	$V_{obs} - V_{exp}$	V	$B - V$	SNR	Rank	Note[b]	Comment[c]
J0042+4132	−255.0	−213.0	−42.0	17.523	0.455	7.7	1	fgd	⋯
LAMOST J0042+4153	−149.5	−349.5	200.0	⋯	⋯	66.8	2	⋯	⋯
J0043+4103	−375.1	−336.7	−38.4	18.719	0.654	10.7	1	⋯	⋯
J0043+4111	−213.0	−309.0	96.0	18.340	0.601	25.9	1	⋯	⋯
J0043+4103	−377.1	−332.0	−45.1	18.071	0.89	12.7	1	A5I	⋯
J0043+4109	−177.6	−309.7	132.1	17.304	1.332	5.6	2	fgd	⋯
J0043+4141	−184.0	−194.5	10.5	16.973	0.632	10.9	1	YSG:	⋯
J0043+4105	−188.7	−315.5	126.8	16.585	0.943	34.3	1	fgd	⋯
LAMOST J0043+4124	−141.5	−53.9	−87.5	⋯	⋯	7.9	1	⋯	⋯
J0043+4153	−171.6	−201.6	30.0	16.541	0.781	8.1	1	fgd	⋯
J0043+4125	−157.3	−64.9	−92.4	18.337	0.678	9.4	1	⋯	⋯
J0043+4122	−180.2	−132.4	−47.8	18.373	0.549	16.2	1	⋯	⋯
J0043+4119	−210.8	−202.0	−8.8	15.467	1.012	6.82	2	fgd	⋯
J0043+4110	−271.6	−287.8	16.2	18.458	0.340	14.5	1	⋯	⋯
J0043+4126	−140.9	−112.9	−28.0	18.328	0.557	15.6	1	⋯	⋯
LAMOST J0043+4207	−281.9	−185.0	−96.9	⋯	⋯	31.2	2	⋯	⋯
LAMOST J0044+4056	−131.5	−310.1	178.7	⋯	⋯	5.3	1	⋯	⋯
J0044+4158	−236.4	−163.5	−72.9	18.856	0.480	7.6	1	⋯	⋯
J0044+4201	−206.2	−165.3	−40.9	15.598	0.462	19.8	1	YSG:	Strong 7774
J0044+4201	−140.1	−160.9	20.9	17.415	0.598	8.3	2	YSG:	⋯
Mag J0044+4116	−228.9	−252.9	24.0	15.150	1.180	21.6	1	fgd	⋯
J0044+4202	−144.0	−160.0	15.7	15.615	0.614	11.3	1	⋯	⋯
J0044+4121	−233.7	−224.8	−8.9	16.727	0.914	12.3	1	YSG:	Strong 7774
J0044+4205	−166.9	−149.2	−17.7	18.078	0.071	11.1	1	⋯	⋯
J0044+4135	−146.2	−84.7	−61.5	15.332	0.569	8.0	1	⋯	⋯
J0044+4133	−132.5	−116.6	−15.9	17.429	0.639	5.8	1	⋯	⋯
J0044+4215	−208.3	−158.4	−49.9	17.355	0.524	10.1	2	⋯	NE
J0044+4123	−182.8	−219.5	36.7	17.574	0.652	7.3	1	YSG:	⋯
LAMOST J0044+4109	−192.9	−272.0	79.1	⋯	⋯	284.9	2	⋯	⋯
J0044+4214	−152.9	−142.8	−10.1	18.705	0.043	5.5	1	⋯	NE
J0045+4130	−388.4	−186.1	−202.3	16.834	0.555	13.1	1	YSG:	⋯
J0045+4226	−193.5	−144.0	−50.0	17.096	0.787	9.1	1	⋯	NE
J0045+4132	−488.8	−187.7	−261.1	15.792	0.853	16.3	1	YSG:	⋯
J0045+4205	−163.2	−74.0	−89.2	17.217	0.740	17.6	1	⋯	⋯
J0045+4136	−166.5	−167.7	1.3	15.877	0.943	5.5	1	YSG:	⋯
J0045+4132	−163.8	−188.1	24.3	16.788	0.600	12.0	2	⋯	⋯
J0045+4229	−185.2	−129.0	−56.2	16.985	0.266	6.9	1	⋯	NE
J0045+4158	−236.4	−54.8	−181.6	16.149	0.647	30.3	2	⋯	⋯
J0045+4133	−377.8	−190.5	−187.2	17.159	0.592	6.2	2	fgd	⋯
J0046+4235	−206.4	−127.1	−79.3	17.746	0.359	6.5	1	⋯	NE
J0046+4231	−146.0	−117.7	−28.3	16.677	0.741	11.6	1	⋯	NE
J0046+4144	−160.2	−150.4	−9.9	15.224	0.654	27.6	1	YSG:	⋯
LAMOST J0046+4214	−230.1	−61.7	−168.4	⋯	⋯	16.3	2	⋯	⋯
LAMOST J0046+4209	−137.5	−56.3	−81.2	⋯	⋯	15.4	1	⋯	⋯
J0046+4208	−150.8	−58.8	−92.0	16.648	0.467	7.5	2	⋯	⋯
LAMOST J0047+4256	−171.3	−122.2	−49.0	⋯	⋯	7.0	1	⋯	NE
J0047+4212	−168.5	−66.6	−101.9	17.302	0.723	6.8	1	⋯	⋯
J0047+4232	−143.6	−64.6	−79.0	16.593	0.292	7.3	1	⋯	NE
LAMOST J0048+4208	−136.2	−106.6	−29.6	⋯	⋯	15.1	1	⋯	⋯
LAMOST J0048+4238	−132.8	−59.1	−73.7	⋯	⋯	25.0	1	⋯	NE
J0048+4233	−161.1	−53.7	−107.4	17.683	0.466	13.4	1	⋯	NE
LAMOST J0049+4210	−104.9	−143.4	−38.5	⋯	⋯	49.0	2	⋯	⋯
LAMOST J0049+4231	−182.5	−80.7	−101.8	⋯	⋯	109.2	2	⋯	⋯
LAMOST J0049+4252	−155.0	−53.6	−101.4	⋯	⋯	9.05	2	⋯	⋯
LAMOST J0049+4257	−226.1	−53.7	−172.4	⋯	⋯	13.9	2	⋯	⋯

Table A1
(Continued)

Star[a]	V_{obs}	V_{exp}	$V_{obs} - V_{exp}$	V	$B - V$	SNR	Rank	Note[b]	Comment[c]
				Red Supergiants					
J0041+4110	−390.0	−407.1	17.1	19.626	2.215	5.4	1	RSG	Massey+2021
J0043+4114	−286.1	−263.0	−23.1	19.935	2.438	5.7	1	RSG	Massey+2021
J0044+4155	−136.3	−116.9	−19.3	16.773	2.046	5.1	1	fgd	⋯

Notes. A more detailed version, including R.A., decl., and LAMOST observation times with SNR > 5, is available in electronic form in the online version of this manuscript (see beginning of Section 4).
[a] Objects selected from LGGS are provided with LGGS names, while those from Magnier et al. (1992) or Gaia are labeled with Mag or LAMOST as a prefix before the coordinates.
[b] (1) "Massey members" are provided with the spectral type from Massey et al. (2016). (2) "Massey non-members" are noted as "fgd."
[c] (1) LBV identified by Huang et al. (2019) is added as a comment "Huang+2019." (2) BSGs analyzed by Liu et al. (2022) based on the spectroscopic method are added as a comment "Liu+2022." (3) Candidates located within the substructure in the northeastern (southwestern) corner of M31 (M33) are added as a comment "NE (SW)." (4) RSGs identified by Massey et al. (2021) using NIR photometry are added as a comment "Massey+2021." (5) YSGs observed with the O I λ7774 triplet in LAMOST spectra will be commented.

Table A2
84 Supergiants in M33

Star	V_{obs}	V_{exp}	$V_{obs} - V_{exp}$	V	$B - V$	SNR	Rank	Note	Comment
				Blue Supergiants					
J0132+3034	−116.6	−146.8	30.2	18.939	−0.005	5.3	1	⋯	⋯
J0132+3024	−140.5	−115.8	−24.7	15.406	0.258	17.0	1	⋯	Liu+2022
J0132+3038	−127.7	−160.3	32.6	16.727	0.010	14.4	1	B3I	⋯
J0132+3031	−121.7	−127.3	5.6	17.817	0.135	6.1	1	⋯	⋯
J0133+3048	−118.4	−202.5	84.1	16.494	0.113	23.4	1	WNE+B3	⋯
J0133+3020	−151.1	−105.1	−46.0	18.284	−0.096	6.0	1	B4I	⋯
J0133+3030	−141.6	−100.6	−41.0	18.628	−0.076	5.1	1	⋯	⋯
J0133+3036	−152.4	−100.1	−52.3	16.904	0.031	7.5	1	A6III	⋯
J0133+3032	−153.2	−116.7	−36.4	17.194	0.034	12.0	1	B9	⋯
J0133+3027	−169.8	−122.1	−47.7	17.613	−0.049	5.6	1	⋯	⋯
J0133+3027	−184.9	−125.5	−59.4	18.941	0.023	8.7	1	F0I	⋯
J0133+3022	−122.1	−123.4	1.3	18.657	−0.051	5.2	1	⋯	⋯
J0133+3023	−146.7	−123.5	−23.2	17.183	0.099	6.1	1	A0Ia+Neb	⋯
J0133+3023	−145.1	−123.8	−21.3	16.395	0.009	12.6	1	B8Iae	⋯
J0134+3044	−263.0	−262.2	−0.8	15.412	0.170	37.6	1	⋯	Liu+2022
J0134+3036	−148.5	−166.0	17.5	18.145	−0.018	9.7	1	⋯	Liu+2022
J0134+3044	−202.6	−224.2	41.6	18.166	0.086	8.4	1	⋯	⋯
J0134+3041	−166.9	−217.1	50.1	18.468	−0.160	7.2	1	O9.5I	⋯
J0134+3033	−139.1	−166.4	27.3	16.837	0.131	8.0	1	cLBV	⋯
J0134+3034	−150.1	−172.7	22.5	18.969	0.259	7.7	1	cLBV	⋯
J0134+3039	−171.3	−201.6	30.3	17.143	0.044	21.3	1	B9I	⋯
J0134+3035	−156.2	−179.4	23.2	18.366	−0.059	11.2	1	B3I	⋯
J0134+3049	−327.8	−252.3	−75.5	18.381	−0.058	11.7	1	⋯	⋯
J0134+3051	−193.1	−253.	60.6	18.622	−0.05	6.7	1	⋯	⋯
J0134+3046	−229.7	−233.2	3.5	17.296	−0.005	12.2	1	B5I	⋯
J0134+3027	−138.3	−159.9	21.6	18.069	0.111	16.3	1	B8I	⋯
J0134+3056	−246.1	−259.8	13.7	18.299	−0.021	7.2	1	B2I	⋯
J0135+3044	−143.2	−214.8	71.6	17.654	−0.038	13.6	1	B5I	⋯
				Yellow Supergiants					
LAMOST J0131+3018	−163.7	−127.1	−36.6	⋯		17.5	2	⋯	⋯
LAMOST J0131+3005	−133.0	−111.7	−21.3	⋯	⋯	7.3	1	⋯	SW
LAMOST J0131+3028	−219.4	−141.3	−78.1	⋯	⋯	17.3	2	⋯	⋯
LAMOST J0131+3001	−189.5	−105.5	−84.0	⋯	⋯	5.3	2	⋯	SW
J0131+3032	−179.6	−148.2	−31.4	18.557	0.553	6.8	2	⋯	⋯
LAMOST J0131+3041	−126.0	−166.7	40.7	⋯	⋯	11.4	2	⋯	⋯

Table A2
(Continued)

Star	V_{obs}	V_{exp}	$V_{obs} - V_{exp}$	V	$B - V$	SNR	Rank	Note	Comment
J0132+3006	−149.1	−105.7	−43.4	17.001	0.596	11.6	1	⋯	SW
J0132+3014	−121.2	−112.4	−8.8	18.043	0.629	8.8	2	⋯	⋯
J0132+3033	−257.6	−148.9	−108.7	17.730	0.684	7.6	2	fgd	⋯
J0132+3036	−221.3	−155.2	−66.1	17.532	0.580	6.0	2	fgd	⋯
LAMOST J0132+3003	−284.9	−100.5	−184.4	⋯	⋯	7.4	2	⋯	SW
J0132+3022	−137.5	−108.7	−28.8	18.831	0.069	6.4	1	⋯	⋯
J0132+3045	−130.5	−182.3	51.8	14.483	1.098	49.7	2	YSG:	⋯
J0132+3034	−148.2	−140.5	−7.7	17.120	0.141	10.2	1	YSG	⋯
J0132+3029	−131.3	−123.0	−8.4	17.143	0.987	8.1	2	YSG::	⋯
J0133+3052	−120.3	−204.9	84.6	17.436	0.543	6.6	2	fgd	⋯
J0133+3037	−161.8	−151.1	−10.6	18.127	1.230	5.3	1	YSG	⋯
J0133+3034	−118.0	−130.8	12.8	16.454	0.254	10.3	1	F0Ia	⋯
J0133+3025	−127.6	−100.4	−27.2	17.032	0.366	27.3	1	YSG	Strong 7774
J0133+3104	−123.7	−230.1	106.4	17.694	0.710	6.8	2	fgd	⋯
J0133+3026	−138.1	−100.4	−37.6	15.583	0.754	15.1	2	fgd	⋯
J0133+3052	−213.2	−219.3	6.1	18.663	0.059	6.7	1	⋯	⋯
J0133+3005	−199.1	−106.7	−92.5	16.850	0.610	5.1	2	YSG::	⋯
J0133+3038	−194.7	−155.1	−39.7	18.159	0.726	10.1	1	⋯	⋯
J0133+3057	−202.1	−231.1	29.0	18.703	0.009	5.6	1	⋯	⋯
J0133+3041	−135.6	−190.0	54.4	17.372	0.899	11.4	2	⋯	⋯
J0133+3022	−164.9	−106.0	−58.9	16.742	0.295	5.6	1	YSG	⋯
J0133+3035	−130.4	−105.3	−25.2	17.937	0.062	21.3	1	A5I	⋯
J0133+3031	−135.3	−100.7	−34.7	16.201	0.739	6.8	1	G0Ia	⋯
J0133+3052	−283.7	−244.9	−38.8	17.645	0.120	5.6	1	A4I	⋯
J0133+3100	−234.9	−250.3	15.4	16.774	0.310	9.3	1	YSG	⋯
J0133+3009	−152.3	−119.6	−32.7	17.789	0.551	9.8	2	YSG::	⋯
J0134+3050	−116.8	−261.4	144.6	17.029	0.656	26.3	2	⋯	⋯
J0134+3107	−166.4	−255.0	88.6	17.058	0.705	9.5	2	fgd	⋯
J0134+3040	−156.5	−208.8	52.3	15.825	1.073	6.8	1	fgd	⋯
J0134+3046	−210.2	−260.6	50.4	15.996	0.332	13.1	1	YSG	Strong 7774
J0134+3028	−173.2	−144.4	−28.8	17.284	0.854	20.4	1	F0Ie	⋯
J0134+3047	−256.0	−259.6	3.6	18.926	0.324	7.7	1	⋯	⋯
J0134+3036	−168.2	−176.7	8.4	18.722	0.204	9.0	1	⋯	⋯
J0134+3055	−220.3	−263.7	43.4	16.905	0.246	10.5	1	YSG	Weak 7774
J0134+3046	−263.5	−252.4	−11.0	16.868	0.252	7.4	1	YSG	⋯
J0134+3057	−153.0	−263.6	110.6	17.037	0.705	5.5	2	fgd	⋯
J0134+3041	−165.4	−211.5	46.2	16.765	0.225	5.6	1	A8Ia	⋯
J0134+3038	−215.5	−197.6	−17.9	17.061	0.286	19.2	1	YSG	7774
J0134+3026	−269.7	−161.6	−108.1	16.058	0.814	35.1	2	fgd	⋯
J0134+3054	−257.3	−254.9	−2.4	18.203	0.084	6.1	1	YSG	⋯
J0134+3041	−145.7	−209.1	63.4	16.468	0.854	9.1	2	YSG:	⋯
J0135+3058	−135.3	−254.1	118.8	15.474	0.771	22.2	2	fgd	⋯
J0135+3105	−345.6	−257.1	−88.5	17.567	0.440	15.3	2	fgd	⋯
J0135+3105	−115.5	−255.4	139.9	15.963	0.567	8.6	2	fgd	⋯
J0135+3048	−112.9	−223.2	110.3	17.520	0.586	18.5	2	fgd	⋯
LAMOST J0135+3109	−168.6	−257.5	88.9	⋯	⋯	17.4	2	⋯	⋯
LAMOST J0135+3058	−147.3	−239.7	92.4	⋯	⋯	25.4	2	⋯	⋯
				Red Supergiants					
J0133+3030	−127.8	−114.0	−13.7	18.056	2.061	6.5	1	RSG	⋯
J0133+3100	−198.9	−222.8	23.9	16.002	1.621	14.3	1	RSG	⋯
J0134+3048	−263.5	−262.0	−1.5	17.983	1.949	7.3	1	M2-3Ia:	⋯

Note. A more detailed version, including R.A., decl., and LAMOST observation times with SNR > 5, is available in electronic form in the online version of this manuscript.

References

Azimlu, M., Marciniak, R., & Barmby, P. 2011, AJ, 142, 139
Bohannan, B. 1997, in ASP Conf. Ser. 120, Luminous Blue Variables: Massive Stars in Transition, ed. A. Nota & H. Lamers (San Francisco, CA: ASP), 3
Braun, R., Thilker, D. A., Walterbos, R. A. M., & Corbelli, E. 2009, ApJ, 695, 937
Chen, B.-Q., Liu, X.-W., Xiang, M.-S., et al. 2015, RAA, 15, 1392
Chen, Y., Girardi, L., Fu, X., et al. 2019, A&A, 632, A105
Ciardullo, R., Durrell, P. R., Laychak, M. B., et al. 2004, ApJ, 614, 167
Conti, P. S. 1997, in ASP Conf. Ser. 120, Luminous Blue Variables: Massive Stars in Transition, ed. A. Nota & H. Lamers (San Francisco, CA: ASP), 387
Cui, X.-Q., Zhao, Y.-H., Chu, Y.-Q., et al. 2012, RAA, 12, 1197
Deng, L.-C., Newberg, H. J., Liu, C., et al. 2012, RAA, 12, 735
Drout, M. R., Massey, P., & Meynet, G. 2012, ApJ, 750, 97
Drout, M. R., Massey, P., Meynet, G., Tokarz, S., & Caldwell, N. 2009, ApJ, 703, 441
Eggenberger, P., Ekström, S., Georgy, C., et al. 2021, A&A, 652, A137
Ekström, S., Georgy, C., Eggenberger, P., et al. 2012, A&A, 537, A146
Fritz, J., Gentile, G., Smith, M. W. L., et al. 2012, A&A, 546, A34
Galleti, S., Federici, L., Bellazzini, M., Fusi Pecci, F., & Macrina, S. 2004, A&A, 416, 917
Galleti, S., Bellazzini, M., Federici, L., Buzzoni, A., & Fusi Pecci, F. 2007, A&A, 471, 127
Galleti, S., Bellazzini, M., Buzzoni, A., Federici, L., & Fusi Pecci, F. 2009, A&A, 508, 1285
Gao, H., Zhang, H.-W., Xiang, M.-S., et al. 2015, RAA, 15, 2204
Hartmann, D., & Burton, W. B. 1997, Atlas of Galactic Neutral Hydrogen (Cambridge: Cambridge Univ. Press), 243
Hodge, P. W., Balsley, J., Wyder, T. K., & Skelton, B. P. 1999, PASP, 111, 685
Huang, Y., Liu, X. W., Chen, B. Q., et al. 2018, AJ, 156, 90
Huang, Y., Yuan, H., Li, C., et al. 2021, ApJ, 907, 68
Huang, Y., Zhang, H. W., Wang, C., et al. 2019, ApJL, 884, L7
Jarrett, T. H., Chester, T., Cutri, R., Schneider, S. E., & Huchra, J. P. 2003, AJ, 125, 525
Kurucz, R. L. 1992, in The Stellar Populations of Galaxies (IAUS 149) ed. B. Barbuy & A. Renzini (Cambridge: Cambridge Univ. Press), 225
Li, Q.-Z., Huang, Y., Dong, X.-B., Chen, J.-J., & Luo, A. L. 2023, RAA, 23, 115026
Liu, C., Kudritzki, R.-P., Zhao, G., et al. 2022, ApJ, 932, 29
Liu, X. W., Yuan, H. B., Huo, Z. Y., et al. 2014, in Setting the Scene for Gaia and LAMOST (IAUS 298) ed. S. Feltzing et al. (Cambridge: Cambridge Univ. Press), 310
Luo, A. L., Zhao, Y.-H., Zhao, G., et al. 2015, RAA, 15, 1095
Magnier, E. A., Lewin, W. H. G., van Paradijs, J., et al. 1992, A&AS, 96 379
Massey, P. 1998, ApJ, 501, 153
Massey, P. 2013, NewAR, 57, 14
Massey, P., McNeill, R. T., Olsen, K. A. G., et al. 2007, AJ, 134, 2474
Massey, P., Neugent, K. F., Levesque, E. M., Drout, M. R., & Courteau, S. 2021, AJ, 161, 79
Massey, P., Neugent, K. F., & Smart, B. M. 2016, AJ, 152, 62
Massey, P., & Olsen, K. A. G. 2003, AJ, 126, 2867
Massey, P., Olsen, K. A. G., Hodge, P. W., et al. 2006, AJ, 131, 2478
Massey, P., Silva, D. R., Levesque, E. M., et al. 2009, ApJ, 703, 420
Neugent, K. F., Massey, P., Skiff, B., Drout, M. R., Meynet, G., & Olsen, K. A. G. 2010, ApJ, 719, 1784
Oey, M. S., & Clarke, C. J. 2009, Massive stars: Feedback effects in the local universe, Massive Stars (Cambridge: Cambridge Univ. Press), 74
Osmer, P. S. 1972, ApJS, 24, 247
Przybilla, N., Butler, K., Becker, S. R., Kudritzki, R. P., & Venn, K. A. 2000, A&A, 359, 1085
Salomon, J. B., Ibata, R., Reylé, C., et al. 2021, MNRAS, 507, 2592
Sanders, N. E., Caldwell, N., McDowell, J., & Harding, P. 2012, ApJ, 758 133
Sarajedini, A., & Mancone, C. L. 2007, AJ, 134, 447
Smith, N. 2014, ARA&A, 52, 487
van den Bergh, S. 2000, The Galaxies of the Local Group (Cambridge: Cambridge Univ. Press)
Yan, H., Li, H., Wang, S., et al. 2022, Innov, 3, 100224
Yuan, H.-B., Liu, X.-W., Huo, Z.-Y., et al. 2010, RAA, 10, 599
Yuan, H. B., Liu, X. W., Huo, Z. Y., et al. 2015, MNRAS, 448, 855
Yusof, N., Hirschi, R., Eggenberger, P., et al. 2022, MNRAS, 511, 2814
Zhang, M., Chen, B.-Q., Huo, Z.-Y., et al. 2020, RAA, 20, 097
Zhao, G., Zhao, Y.-H., Chu, Y.-Q., Jing, Y.-P., & Deng, L.-C. 2012, RAA, 12, 723